

# Various Barbs in Solar Filaments

Boris Filippov

Pushkov Institute of Terrestrial Magnetism, Ionosphere and Radio Wave Propagation of the Russian Academy of Sciences (IZMIRAN), Troitsk, Moscow 108840, Russia  
 Email: bfilip@izmiran.ru

(RECEIVED May 2, 2017; ACCEPTED June 8, 2017)

## Abstract

Interest to lateral details of the solar filament shape named barbs, motivated by their relationship to filament chirality and helicity, showed their different orientation relative to the expected direction of the magnetic field. While the majority of barbs are stretched along the field, some barbs seem to be transversal to it and are referred to as anomalous barbs. We analyse the deformation of helical field lines by a small parasitic polarity using a simple flux rope model with a force-free field. A rather small and distant source of parasitic polarity stretches the bottom parts of the helical lines in its direction creating a lateral extension of dips below the flux-rope axis. They can be considered as normal barbs of the filament. A stronger and closer source of parasitic polarity makes the flux-rope field lines to be convex below its axis and creates narrow and deep dips near its position. As a result, the narrow structure, with thin threads across it, is formed whose axis is nearly perpendicular to the field. The structure resembles an anomalous barb. Hence, the presence of anomalous barbs does not contradict the flux-rope structure of a filament.

Keywords: Sun: magnetic fields – Sun: filaments, prominences – Sun: chromosphere – Sun: corona

## 1 INTRODUCTION

Solar filament fine structure consists of thin threads crossing the filament long axis at an acute angle (Lin, Engvold, & Wiik, 2003; Lin et al., 2005; Martin, Lin, & Engvold, 2008). It is widely accepted that threads represent segments of magnetic flux tubes filled with relatively cold and dense plasma absorbing or emitting radiation. Thus, the fine structure of a filament shows the direction of magnetic field in different parts of the filament body. Measurements of the magnetic field in prominences (Bommier & Leroy, 1998; Trujillo Bueno et al., 2002) confirm information obtained from analysis of solar images. Usually the magnetic field vector is pointed about 25–30° away from the filament long axis. The angle changes from filament to filament and within the same filament. The direction of threads near the upper boundary of a filament, called the spine, is more aligned with the axis. Sometimes a movement of material along the axis nearly through the whole length of the filament manifests the presence of axial flux tubes.

According to the direction of the axial component of the filament magnetic field relative to the surrounding photospheric field distribution, Martin, Bilimoria, & Tracadas (1994) separated all filaments into two kinds: dextral and sinistral. In

dextral (sinistral) filaments, the axial field points to the right (left) when viewed from the positive photospheric polarity. Since measurements of magnetic fields in filaments are rare, the belonging of a particular filament to a definite class (its chirality) can be derived by inspecting of the anchoring of its ends in definite photospheric polarities, or the usage of the direction of filament fine threads and a surrounding fibril pattern (Foukal, 1971; Martin et al., 2008). Dextral filaments are located preferably in the northern hemisphere, while sinistral filaments dominate in the southern hemisphere, and this tendency does not change from a cycle to cycle (Martin et al., 1994; Zirker et al., 1997).

Most of filaments have lateral extensions called barbs (examples are presented in Figure 1). They protrude at an acute angle from the main body of the filament and seemingly terminate in the chromosphere. They can be classified as either right bearing or left bearing depending on the deviation of the barbs from the axis. Martin and colleagues (Martin et al., 1994; Martin & Echols, 1994; Martin, 1998) found that the barbs of a dextral (sinistral) filament are observed to be right (left) bearing in most cases. Owing to this rule, it is possible to estimate the chirality of a filament basing on its morphology without any information about magnetic fields. There were attempts to find photospheric counterparts of barb ends but

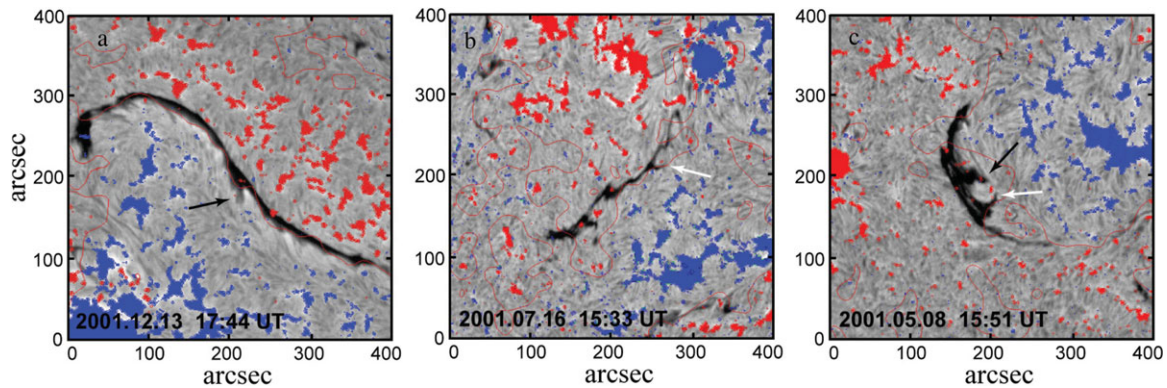


**Figure 1.**  $H\alpha$  filtergrams showing filaments with different types of barbs with superposed SOHO/MDI magnetograms. Red (blue) areas represent negative (positive) polarity. Black arrows point to normal barbs, while white arrows point to anomalous barbs. (Courtesy of the Big Bear Solar Observatory and MDI science team).

results were rather ambiguous. For example, Płoceniak & Rompolt (1973) reported that barbs terminated at junctions of supergranular cells, van Ballegoijen (2004) found the association of a barb with a weak-field extension of a neighbouring network element of parasitic polarity, while Martin et al. (1994), Martin & Echols (1994), and Wang (2001) associated barbs with weak parasitic polarities distinct from network elements. Many authors related barb ends to small-scale polarity inversion lines (PILs) created by parasitic polarity patches (Zong et al., 2003; Chae, Moon, & Park, 2005; Lin et al., 2005). Filippov (2016) showed that many barbs lay within areas enveloped by PILs calculated in a potential-field approximation for chromospheric heights.

From magnetostatic point of view, dense filament material should be rested in magnetic dips or sags in field lines (Dungey, 1953; Kippenhahn & Schlüter, 1957). Two magnetic configurations are considered as most favourable for the filament support in the corona. A twisted magnetic flux rope (Kuperus & Raadu, 1974; van Tend & Kuperus, 1978; Pneuman, 1983; Priest, Hood, & Anzer, 1989; Rust & Kumar, 1994; Aulanier & Demoulin, 1998; Gibson & Fan, 2006) has dips in lower parts of helical field lines. The direction of the transversal to the flux-rope axis component of the flux-rope magnetic field in these dips is opposite to the expected direction of the coronal magnetic field created by photospheric sources. Thus, a filament within this configuration has ‘inverse polarity’. Another configuration is a sheared arcade (Antiochos, Dahlburg, & Klimchuk, 1994; DeVore & Antiochos, 2000; Martens & Zwaan, 2001; Aulanier, DeVore, & Antiochos, 2002; Karpen et al., 2003; Mackay & van Ballegoijen, 2005) with dips at tops of sheared magnetic arches. Most of dips in these numerical models have also inverse polarity; however, some dips can be of normal polarity.

If barbs are considered as the lateral extension of thin threads constituting the main filament body, they should stick to the rule deduced by Martin and colleagues in inverse polarity filaments and contradict this rule in normal polarity filaments. Observations indicate that the majority of barbs really stick the chirality rule. However, there exist filaments with

‘anomalous’ barbs (e.g., Figure 1), which according to many evidences belong to a definite class of chirality but have one or several barbs typical for the opposite chirality (Pevtsov, Balasubramaniam, & Rogers 2003; Martin et al. 2008).

Guo et al. (2010) extrapolated in the non-linear force-free approximation the vector magnetic field measurements below a filament on 2005 May 27. They found that one section of the filament had the structure of a flux rope, while the other was a sheared arcade. Dips in the flux rope have inverse polarity and are able to form normal barbs, whereas dips in the arcade are of normal polarity and can make up anomalous barbs. Nevertheless, the chirality (and helicity) is the same in both sections of the filament in this model despite the different barb bearing. In some works, the observation of both right-bearing and left-bearing barbs in one filament led to the conclusion of different helicity signs in different parts of the filament (Chandra et al., 2010). To avoid subjective judgement of the filament chirality based on general orientation of majority of barbs, Pevtsov et al. (2003) suggested computing a fractional chirality as a weighted difference between the numbers of normal and anomalous barbs. Hao et al. (2016) used an automatic method for detecting the filament chirality and barb bearing. On a sample of four filaments, they concluded the absence of one-to-one correspondence between filament chirality and barb bearing. However, their method of the filament endpoint localisation in magnetic polarities seems not too reliable, because they use magnetic maps with mixture of small-scale magnetic features. Thus, the endpoints, which can be identified with poor accuracy, may fall into any small polarity patch. Possibly, that is why they identified the filament with exclusively right-bearing barbs on 2011 October 12 as sinistral, while the filament with dominating left-bearing barbs on 2013 February 18 as dextral. Liu, Xu, & Wang (2010) observed changes of barb bearing within periods as short as hours. This fact gives rise to their doubt on reliability of barbs as the indicator of the filament chirality.

Martin et al. (2008) argued that the direction of an anomalous barb may be not along the magnetic field. Observations with better spatial resolution show that such a barb

is composed of thin short threads nearly perpendicular to the axis of the anomalous barb (see their Figure 5). These short threads show the same direction of the field as normal barbs and threads within the filament body. Nevertheless, a question emerges, how such a structure can appear in flux-rope models of a filament. In detailed calculations of dip structures made by Aulanier and colleagues (Aulanier & Demoulin, 1998; Aulanier et al., 1998, 1999), all lateral barbs, which appear due to the deformation of the flux-rope magnetic field by small parasitic polarities, are normal apart from the normal polarity configuration with very faint coronal electric current. Possibly at that time, the anomalous barbs did not attract much attention and the authors considered their result with the anomalous barbs as not corresponding to observations.

In this paper, we focus on the shape and orientation of barbs observed from above. On the basis of a simple flux-rope model, we analyse the deformation of helical field lines by a small patch of parasitic polarity. We show that the presence of a faint and distant parasitic polarity leads to appearance of a normal barb. A stronger source of parasitic polarity closer to the flux rope deforms the flux-rope field lines in such a way that a structure resembling an anomalous barb arises.

## 2 EXAMPLES OF BARBS

Figure 1 presents examples of filaments with barbs oriented in different ways, relatively filament long axes and general directions of thin threads within filament bodies. In all panels of Figure 1, magnetograms obtained with the Michelson Doppler Imager [MDI; Scherrer et al. (1995)] on board the Solar and Heliospheric Observatory (SOHO) are superposed on  $H\alpha$  filtergrams. Red and blue areas represent negative and positive polarities with the field strength more than 100 G, respectively. Thin solid red lines show large-scale PILs calculated after Gaussian averaging of magnetograms over a radius of 10–15 arcsec. This averaging is necessary to recognise magnetic details of the size of barbs. Wider averaging would show larger scale PILs, which are closer to filament spines. A filament in Figure 1 a is evidently dextral according the direction of its thin threads and visible locations of its ends. All barbs of the filament are normal. Most dark (dense) barbs are related to small patches of positive (parasitic) polarity on the southern side of the filament. The PIL bends around the barbs as it was found in Filippov (2016). A filament in Figure 1 b is sinistral, its northern end approaches to a big positive sunspot, while the dominant polarity on the south-western side of the filament is also positive. Although the northern endpoint is on the negative side of the shown PIL and the southern endpoint is on the positive side of the PIL due to small-scale patches of positive polarity near the southern endpoint and negative near the northern endpoint, this do not disrupt the larger scale distribution of positive polarity at the northern endpoint and negative polarity at the southern endpoint. The shape of the PIL is much curved and depends significantly on averaging. Thin filament threads and

fibrils below the filament deviate counterclockwise from the filament axis as it should be in a sinistral filament. Fibrils somewhat farther to the south-west from the filament have different orientation and form together with the nearest fibrils a ‘herring-bone structure’ (Filippov, 2013), which confirms the derived direction of the field. However, there are two barbs that are right bearing (anomalous). The axis of the most prominent anomalous barb, pointed to by the white arrow, follows the local winding of the PIL. A filament in Figure 1 c is also sinistral. Two adjacent barbs form a semi-circular structure resembling two fingers showing the ‘OK’ sign. The northern barb is left bearing (normal), while the southern one is right bearing (anomalous). The normal barb lies within the area of parasitic polarity although rather far from the PIL encircling it. The southern anomalous barb lies again on the local winding of the PIL. Such pairs of oppositely bearing barbs are not rarely observed in solar filaments. Sometimes they touch each other forming a closed circle.

## 3 SIMPLE MODEL FOR A FLUX ROPE ABOVE THE PHOTOSPHERE

We will proceed from the assumption that the filament magnetic structure can be considered as a flux rope and most of thin threads constituting the filament body and barbs represent lower parts of helical magnetic field lines. Anomalous barbs (see, e.g., Figure 1), which appear sometimes in the structure of filaments, should be features that reflects special conditions in the distribution of the photospheric fields less typical than conditions leading to the creation of normal barbs.

We use a simple model of a force-free flux rope embedded into a horizontal magnetic field above a flat surface (photosphere) with the ideal conductivity (Molodenskii & Filippov, 1988). In the cylindrical coordinate system  $\rho, \varphi, y'$  with the  $y'$  axis directed tangentially the surface of the photosphere, the component of the magnetic field can be expressed in the form

$$B_y^f = c \sin \varphi J_1(\alpha \rho), \quad (1)$$

$$B_\rho^f = c \frac{1}{\alpha \rho} \cos \varphi J_1(\alpha \rho), \quad (2)$$

$$B_\varphi^f = -c \sin \varphi \left( J_0(\alpha \rho) - \frac{1}{\alpha \rho} J_1(\alpha \rho) \right), \quad (3)$$

where  $J_0$  and  $J_1$  are the Bessel functions of the first kind of the zero and first order,  $\alpha$  is the force-free parameter,  $c$  is the field amplitude. They are related to the Cartesian coordinates  $x, y, z$  with the same  $y$  axis and vertical  $z$  axis as usual

$$B_x^f = B_\rho^f \cos \varphi - B_\varphi^f \sin \varphi, \quad (4)$$

$$B_y^f = B_y^f, \quad (5)$$

$$B_z^f = B_\rho^f \sin \varphi + B_\varphi^f \cos \varphi, \quad (6)$$

$$\rho = \sqrt{x^2 + z^2}, \quad (7)$$

$$\sin \varphi = \frac{z}{\rho}. \quad (8)$$

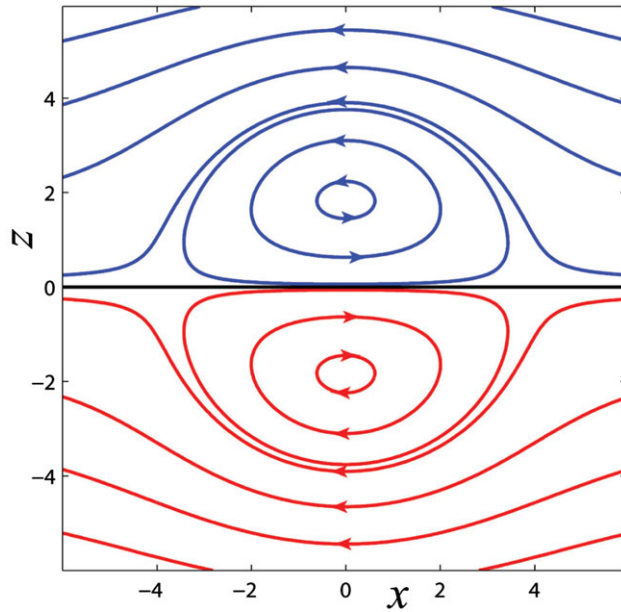


**Figure 2.** Projection of field lines of the flux-rope model onto the  $xz$  plane. Blue lines show the coronal field, red lines are their mirror image.

This field can be joined with the external potential field composed from a horizontal homogeneous field  $B_0$  directed opposite the  $x$  axis and a 2D dipole  $m$  (with the translational symmetry along the  $y$  axis)

$$B_x^m = m \left( \frac{2z^2}{\rho^4} - \frac{1}{\rho^2} \right), \quad (9)$$

$$B_z^m = -m \frac{2xz}{\rho^4}. \quad (10)$$

From the condition of continuity of the field at the joining surface  $\alpha\rho = 3.83$  (the first root of the Bessel function  $J_1$ ), one can obtain (Molodenskii & Filippov, 1988)

$$c = -\frac{2B_0}{0.402}, m = -\frac{3.83^2 B_0}{\alpha^2}. \quad (11)$$

Parameter  $\alpha$  plays a role of scaling; we can set it as  $\alpha = 1$ . The structure of field lines is shown in Figure 2. The pattern is symmetric relative the plane  $z = 0$ , and we can consider the field below this plane as the mirror image of the coronal field.

Then we add to this 2.5D flux-rope model a compact source of parasitic polarity in the form of a linear force-free field solution with a singularity on the negative part of the  $z$ -axis, which in the spherical coordinates  $r_1, \theta_1, \varphi_1$  with the origin at the point  $(x_1, y_1, z_1)$  and the vertical  $z$ -axis has the form Demoulin & Priest (1992)

$$B_{r_1}^q = q \frac{\cos(\alpha r_1 - \varphi_r)}{(\alpha r_1)^2}, \quad (12)$$

$$B_{\theta_1}^q = q \frac{\sin(\alpha r_1 - \varphi_r)}{(\alpha r_1)} \tan\left(\frac{\theta_1}{2}\right), \quad (13)$$

$$B_{\varphi_1}^q = q \frac{\cos(\alpha r_1 - \varphi_r)}{(\alpha r_1)} \tan\left(\frac{\theta_1}{2}\right), \quad (14)$$

where  $r_1 = \sqrt{(x - x_1)^2 + (y - y_1)^2 + (z - z_1)^2}$ ,  $q$  is the amplitude, and  $\varphi_r$  is an arbitrary constant. Aulanier et al. (1998) used the same solution in their analysis of the influence of a parasitic polarity on a flux rope. If the value of  $\alpha$  is the same as in the flux rope (1)–(3), the combined field is also force free. This condition limits to a certain extent the size of the parasitic polarity but choosing appropriate  $z_1$  and  $\varphi_r$ , it is possible to model typical observed situations. We set  $\varphi_r = -\pi/2$  that gives a smoother distribution of the  $B_z$  component.

#### 4 FLUX ROPE DEFORMATIONS

The presence of the parasitic polarity deforms the flux-rope field lines passing over it. Figure 3 presents results of calculations for three different positions of the parasitic polarity at four heights. The left column corresponds to values of parameters  $x_1 = 2, q = -0.2$ ; the middle column  $x_1 = 1, q = -0.25$ ; the right column  $x_1 = 0, q = -0.2$ . Other parameters are the same in all panels:  $c = 1, y_1 = 0, z_1 = -0.1$ . Arrows show the distribution of the horizontal field at different heights, thick red lines represent PILs, black solid lines show limits around PILs where field lines inclined less than  $3^\circ$  to the surface, tinted with green colour areas indicate places where PILs have dips according to expression (Aulanier & Demoulin, 1998)

$$B_x \frac{\partial B_z}{\partial x} + B_y \frac{\partial B_z}{\partial y} > 0. \quad (15)$$

Since  $B_z^q$  changes its sign somewhere about a distance of 2 from the epicentre of the source, the PILs deviates to both sides from the line  $x = 0$  at different distances from  $y = 0$ . We choose the minimum height  $z = 0.5$  for our representation because  $B_y^f$  vanishes at  $z = 0$ , which seems inappropriate for the filament structure. When the parasitic source is most distant from the flux rope (the left column of Figure 3), there is the circular PIL above the source, which encloses the parasitic polarity. Most part of the circular PIL does not lie in a green area and therefore has no dips. Only the right-upper quarter of the circular PIL has dips. We draw the segments of straight lines directed along the horizontal field component  $B_r$  within the limits  $B_z/B_r < .05$ , i.e., the tilt of the field lines to the photosphere is less than  $3^\circ$ , as it is shown in Figure 3. Combinations of these segments at all heights are shown in the bottom row of Figure 3. They should represent the structure of the filament viewed from above. The structure in the left column looks like a dextral filament with a right-bearing barb. At the height of 0.5, there are long lines protruding from the main PIL in the direction of the parasitic polarity. Although the parasitic polarity is surrounded mostly by convex field lines, it deforms the bottom sections of the helical field lines of the flux rope and makes them flatter. The filament material can spread laterally along shallow dips forming a right-bearing barb. This effect was clearly shown by Aulanier et al. (1999). The end of the barb is curved along the circular PIL, but it is very thin and could be not observable. At greater heights, the influence of the parasitic polarity is small.

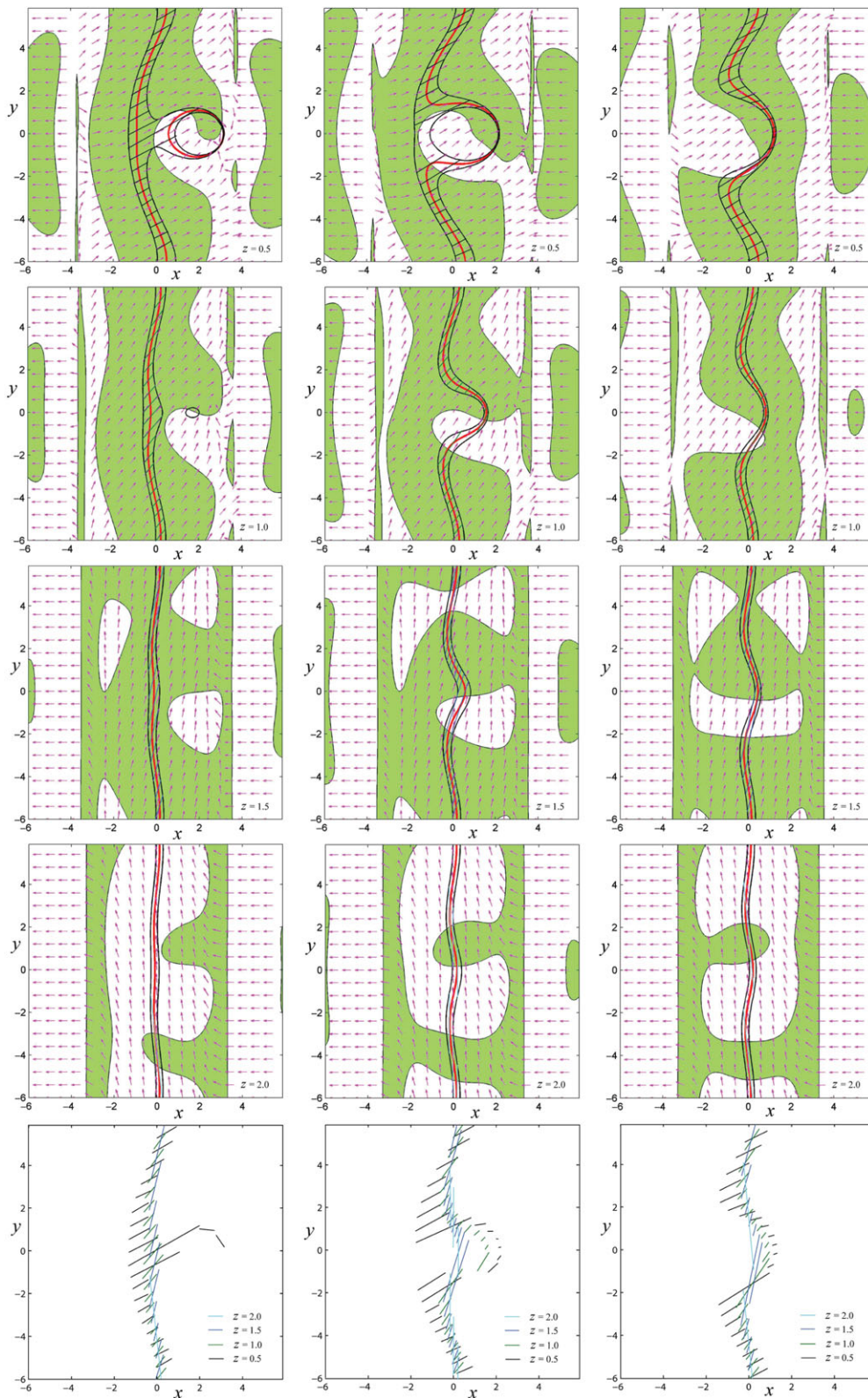


**Figure 3.** Distributions of horizontal field directions (arrows), PILs (thick red lines) at different heights above the photosphere, and aggregates of segments of the field lines with low inclination to the surface (bottom row). Black solid lines show limits around PILs where field lines are inclined less than  $3^\circ$  to the surface. Tinted with green colour areas indicate places where PILs have dips. The left column corresponds to the values of parameters  $x_1 = 2$ ,  $q = -0.2$ ; the middle column  $x_1 = 1$ ,  $q = -0.25$ ; the right column  $x_1 = 0$ ,  $q = -0.2$ .

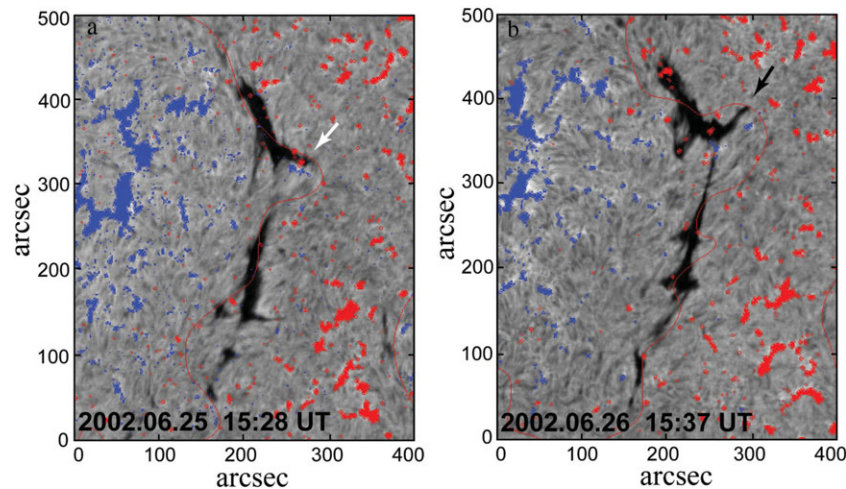


**Figure 4.**  $H\alpha$  filtergrams showing a dextral filament with an anomalous barb on 2002 June 25, which transformed into a normal barb on the next day, with superposed SOHO/MDI magnetograms. Red (blue) areas represent negative (positive) polarity. Thin solid red lines show large-scale PILs. The white arrow points to the anomalous barb, while the black arrow points to the normal barb. (Courtesy of the Big Bear Solar Observatory and MDI science team).

If the source is closer to the flux rope and a little bit stronger ( $x_1 = 1$ ,  $q = -0.25$ ), the circular PIL merges with the linear PIL (the middle column of Figure 3). The upper (in the panel) part of the semi-circular PIL has dips, while its lower part has no dips. Since the section of the linear flux-rope PIL near the parasitic polarity disappears, there are no long lines corresponding to very shallow wide dips. On the other hand, narrow dips in the upper part of the semi-circular PIL form a prominent curved structure, the general direction of which is nearly perpendicular to the direction of the horizontal component of the flux-rope field at this height. The structure resembles an anomalous filament barb. The narrow dips can contain only short threads of material transversal to the axis of the structure as it is observed in anomalous barbs with high resolution.

If the source is just below the flux rope axis ( $x_1 = 0$ ,  $q = -0.2$ ), the PIL of the total field bends smoothly around the parasitic polarity (the right column of Figure 3). The shapes of the PILs are very similar to ones shown in the middle column but the inclination of the lower part of the semi-circular PIL to the  $y$  axis is nearly the same as the inclination of the horizontal field at every height. Thus, flat field lines from dips below the flux-rope axis spread along the lower part of the semi-circular PIL. As a result, the whole semi-circular PIL contains the filament material forming a semi-circular barb. In the upper part, threads are short and are transversal to the direction of the PIL. In the lower part, they are long and directed along the PIL.

## 5 BARBS AND PHOTOSPHERIC MAGNETIC BACKGROUND

Figure 4 presents a filament observed on two successive days, 2002 June 25 and 26. SOHO/MDI magnetograms are super-

posed on  $H\alpha$  filtergrams in the same way as in Figure 1. The filament is dextral but it has a prominent left-bearing (anomalous) barb in the northern part pointed to by the white arrow in Figure 4 a. On the next day, the barb in the same place becomes normal (Figure 4b, black arrow). It is difficult to associate the endpoints of the filaments in Figure 4 with definite polarities but the fine structure of the filaments are clearly visible, and thin threads and fibrils below the filament deviate clockwise from the filament axis as it should be in a dextral filament. The photospheric magnetic field distribution slightly changed during the period between the two snapshots. The normal barb lies within the area of parasitic polarity, the anomalous barb traces the border of the area, the PIL.

Another example of the dextral filament with a barb, being normal on one day and anomalous on another day, is shown in Figure 5. Observations with the Atmospheric Imaging Assembly [AIA; Lemen et al. (2012)] on board the Solar Dynamic Observatory (SDO) provide images with 1.5 arcsec spatial resolution and 0.6 arcsec pixel size. The images in the SDO/AIA 193 Å channel allow one to recognise that the anomalous barb observed in the filament on 2014 August 06 (Figure 5 d) consists of thin threads directed transverse to the axis of the structure like in the high-resolution images presented by Lin et al. (2005) and Martin et al. (2008). Two days before, on August 04, the barb at the same place in the filament looks like normal (Figure 5 a, b). In the panels (b) and (d), magnetograms taken by Heliospheric and Magnetic Imager (HMI; Schou et al. (2012)) on board SDO are superposed on SDO/AIA 193 Å images. PILs are green in these images for better contrast. Figure 5d persuades that the anomalous barb precisely follows the PIL. The normal barb on August 04 lies within the PIL contour. The parasitic polarity in this case has lesser strength.

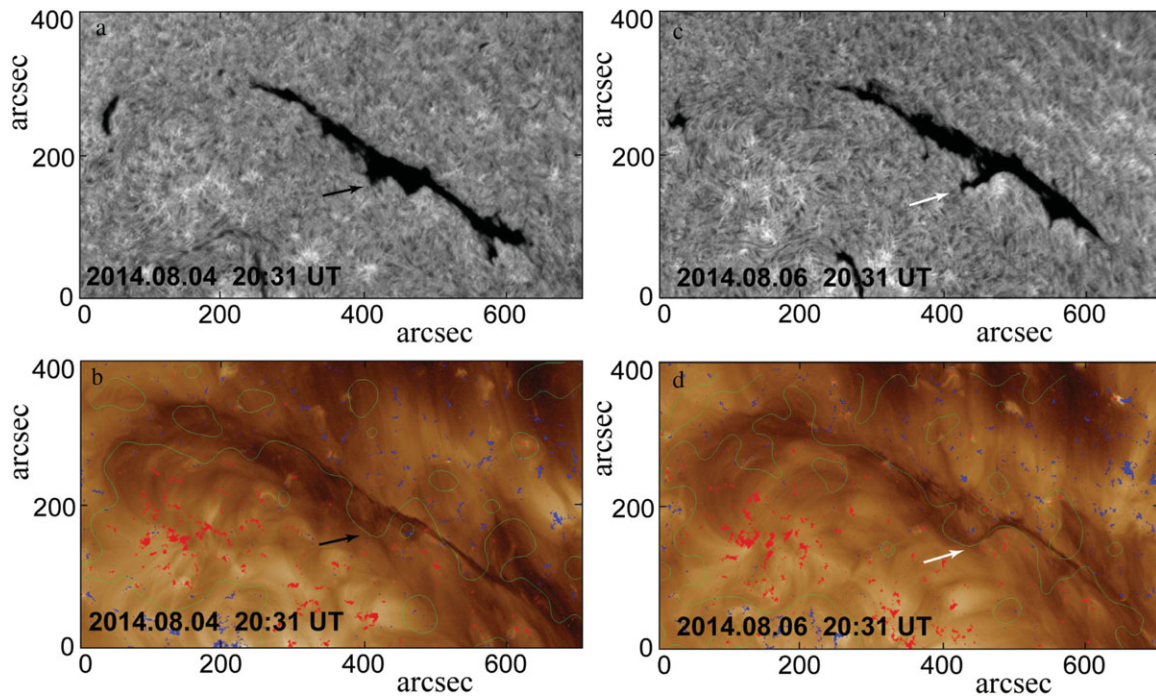


**Figure 5.** Filament in  $H\alpha$  line and 193 Å on 2014 August 04 and 06. SDO/HMI magnetograms are superposed on SDO/AIA 193 Å images in the panels (b) and (d) (red patches correspond to negative polarity, blue ones represent positive polarity). Thin solid green lines show large-scale PILs. The black arrow points to the normal barb, while the white arrow points to the anomalous barb. (Courtesy of the SDO/AIA and SDO/HMI science teams).

Comparison of our model with observations can be only qualitative because of the sketchiness of the former. However, the model reflects some regularity that manifests itself in the presented examples. First, the same flux rope can demonstrate both right-bearing and left-bearing barbs depending on the distribution of the parasitic polarities in the filament channel. Second, the normal barbs are created by rather distant from the flux rope parasitic polarity patches. The barbs lie within areas encircled by PILs. Third, the anomalous barbs are located on borders of parasitic polarity areas. They follow exactly PILs and lie over parts of semi-circular PILs that make greater angles with horizontal magnetic fields.

## 6 CONCLUSION

We analysed the deformation of helical field lines by a small parasitic polarity using a simple flux rope model with a force-free field. Smaller parasitic polarity stretches the bottom parts of the helical lines in its direction creating a lateral extension of dips below the flux-rope axis. They can be considered as normal barbs of the filament. If the strength of the source of parasitic field is greater and it is closer to the flux rope, the flux-rope field lines become convex below its axis. At the same time, the dips above the parasitic polarity get narrower and deeper. The dips are located over the part of the curved PIL that turns round the parasitic polarity and is directed transverse to the direction of the magnetic field. As a result, a narrow structure with thin threads across it is formed, which axis is nearly perpendicular to the field. The

structure resembles an anomalous barb. Hence, the presence of anomalous barbs does not contradict the flux-rope structure of the filament. They can arise under the influence of rather strong parasitic polarities. There is no need to engage too complicated magnetic configuration with a part of the filament as a flux rope and other part as a sheared arcade to explain the observations.

Anomalous barbs are observed not so rarely in solar filaments, but they are less numerous and have lesser lifetimes than the normal barbs (Pevtsov et al., 2003; Martin et al., 2008; Chandra et al., 2010; Liu et al., 2010; Hao et al., 2016). Taking into account their directions could lead to wrong conclusions on the chirality and helicity of a part or the whole filament. However, observation with a little bit better resolution than it is in current routine full-disc  $H\alpha$  observations would show clearly the direction of the constituting threads, which do not contradict the chirality of the other parts of the filament.

## ACKNOWLEDGEMENTS

The author thanks the Big Bear Solar Observatory and the SOHO/MDI, SDO/AIA, SDO/HMI science teams for the high-quality data supplied.

## REFERENCES

- Antiochos, S. K., Dahlburg, R. B., & Klimchuk, J. A. 1994, *ApJ*, **420**, L41  
 Aulanier, G., & Demoulin, P. 1998, *A&A*, **329**, 1125

- Aulanier, G., Démoulin, P., Mein, N., van Driel-Gesztelyi, L., Mein, P., & Schmieder, B. 1999, *A&A*, **342**, 867
- Aulanier, G., Demoulin, P., van Driel-Gesztelyi, L., Mein, P., & Deforest, C. 1998, *A&A*, **335**, 309
- Aulanier, G., DeVore, C. R., & Antiochos, S. K. 2002, *ApJ*, **567**, L97
- Bommier, V., & Leroy, J. L. 1998, in *ASP Conf. Ser.*, Vol. 150, IAU Colloq. 167: New Perspectives on Solar Prominences, eds. D. F. Webb, B. Schmieder, & D. M. Rust (San Francisco: ASP), 434
- Chae, J., Moon, Y.-J., & Park, Y.-D. 2005, *ApJ*, **626**, 574
- Chandra, R., Pariat, E., Schmieder, B., Mandrini, C. H., & Uddin, W. 2010, *SoPh*, **261**, 127
- Démoulin, P., & Priest, E. R. 1992, *A&A*, **258**, 535
- DeVore, C. R., & Antiochos, S. K. 2000, *ApJ*, **539**, 954
- Dungey, J. W. 1953, *MNRAS*, **113**, 180
- Filippov, B. 2013, *SoPh*, **283**, 401
- Filippov, B. 2016, *MNRAS*, **455**, 1406
- Foukal, P. 1971, *SoPh*, **19**, 59
- Gibson, S. E., & Fan, Y. 2006, *JGRA*, **111**, A12103
- Guo, Y., Schmieder, B., Démoulin, P., Wiegelmann, T., Aulanier, G., Török, T., & Bommier, V. 2010, *ApJ*, **714**, 343
- Hao, Q., Guo, Y., Fang, C., Chen, P.-F., & Cao, W.-D. 2016, *RAA*, **16**, 1
- Karpen, J. T., Antiochos, S. K., Klimchuk, J. A., & MacNeice, P. J. 2003, *ApJ*, **593**, 1187
- Kippenhahn, R., & Schlüter, A. 1957, *ZAp*, **43**, 36
- Kuperus, M., & Raadu, M. A. 1974, *A&A*, **31**, 189
- Lemen, J. R., et al. 2012, *SoPh*, **275**, 17
- Lin, Y., Engvold, O. R., & Wiik, J. E. 2003, *SoPh*, **216**, 109
- Lin, Y., Wiik, J. E., Engvold, O., Rouppe van der Voort, L., & Frank, Z. A. 2005, *SoPh*, **227**, 283
- Liu, R., Xu, Y., & Wang, H. 2010, *MmSAI*, **81**, 796
- Mackay, D. H., & van Ballegoijen, A. A. 2005, *ApJ*, **621**, L77
- Martens, P. C., & Zwaan, C. 2001, *ApJ*, **558**, 872
- Martin, S. F. 1998, *SoPh*, **182**, 107
- Martin, S. F., Bilimoria, R., & Tracadas, P. W. 1994, in *NATO Advanced Science Institutes (ASI) Ser. C*, Vol. 433, eds. R. J. Rutten & C. J. Schrijver (Dordrecht, The Netherlands: Kluwer Academic Publishers), 303
- Martin, S. F., & Echols, C. R. 1994, in *NATO Advanced Science Institutes (ASI) Ser. C*, Vol. 433, eds. R. J. Rutten & C. J. Schrijver (Dordrecht, The Netherlands: Kluwer Academic Publishers), 339
- Martin, S. F., Lin, Y., & Engvold, O. 2008, *SoPh*, **250**, 31
- Molodenskii, M. M., & Filippov, B. P. 1988, *SvAer*, **32**, 202
- Pevtsov, A. A., Balasubramaniam, K. S., & Rogers, J. W. 2003, *ApJ*, **595**, 500
- Płoceniak, S., & Rempel, B. 1973, *SoPh*, **29**, 399
- Pneuman, G. W. 1983, *SoPh*, **88**, 219
- Priest, E. R., Hood, A. W., & Anzer, U. 1989, *ApJ*, **344**, 1010
- Rust, D. M., & Kumar, A. 1994, *SoPh*, **155**, 69
- Scherrer, P. H., et al. 1995, *SoPh*, **162**, 129
- Schou, J., et al. 2012, *SoPh*, **275**, 229
- Trujillo Bueno, J., Landi Degl'Innocenti, E., Collados, M., Merenda, L., & Manso Sainz, R. 2002, *Nature*, **415**, 403
- van Ballegoijen, A. A. 2004, *ApJ*, **612**, 519
- van Tend, W., & Kuperus, M. 1978, *SoPh*, **59**, 115
- Wang, Y.-M. 2001, *ApJ*, **560**, 456
- Zirker, J. B., Martin, S. F., Harvey, K., & Gaizauskas, V. 1997, *SoPh*, **175**, 27
- Zong, W. G., Tang, Y. H., Fang, C., Mein, P., Mein, N., & Xu, A. A. 2003, *A&A*, **412**, 267